Electronic Supplementary Information (ESI)

High-entropy amorphous oxycyanide as an efficient pre-catalyst for oxygen evolution reaction

Wenbin Sun,[a,†] Yameng Wang,[a,†] Shanshan Liu,[b] Fengcai Lei,[a] Junfeng Xie,[a,*] and Bo Tang[a,*]

a College of Chemistry, Chemical Engineering and Materials Science, Key Laboratory of Molecular and Nano Probes (Ministry of Education), Collaborative Innovation Center of Functionalized Probes for Chemical Imaging in Universities of Shandong, Institute of Molecular and Nano Science, Shandong Normal University, Jinan, Shandong, 250014, China. E-mail: xiejf@sdnu.edu.cn; tangb@sdnu.edu.cn.

b *College of Chemical Engineering and Safety, Binzhou University, Binzhou 256603, China*

† These authors contributed equally to this work.

1. Experimental section

1.1 Synthesis of the Prussian blue analogue nanocube precursors

For the synthesis of the quinary ***HE-PBA*** nanocubes, namely, CoFeNiCuMn PBA, equivalent amounts of cationic metal salts (namely, 2 mmol $NiCl_2 \cdot 6H_2O$, 2 mmol $CuCl_2 \cdot 2H_2O$ and 2 mmol $MnCl_2 \cdot 4H_2O$) and 9 mmol trisodium citrate dehydrate were dissolved in 100 mL of distilled water by vigorous stirring. Meanwhile, equivalent amounts of anionic metal salts (namely, 2 mmol $K_3[Co(CN)_6]$ and 2 mmol $K_3[Fe(CN)_6]$) were dissolved in 100 mL of distilled water under stirring. After that, the abovementioned solutions were mixed and stirred vigorously until precipitates can be obtained after reacting for 30 min. The powdery product was then rinsed with distilled water and absolute ethanol for several times, and finally dried under vacuum. For the synthesis of the quaternary, ternary, binary PBAs and unary PB nanocube precursors, the metal salts were modified as following.

CoFeCuMn PBA: The cationic metal salts were modified as 3 mmol $CuCl_2 \cdot 2H_2O$ and 3 mmol $MnCl_2 \cdot 4H_2O$, and the other parameters remain unchanged.

CoFeCu PBA: The cationic metal salts were modified as 6 mmol $CuCl_2 \cdot 2H_2O$, and the other parameters remain unchanged.

CuFe PBA: The cationic metal salts were modified as 6 mmol $CuCl_2 \cdot 2H_2O$, and the anionic metal salts were replaced by 4 mmol $K_3[Fe(CN)_6]$. The other experimental parameters remain unchanged.

FeFe PB: The cationic metal salts were modified as 6 mmol $FeCl_2 \cdot 4H_2O$, and the anionic metal salts were replaced by 4 mmol $K_3[Fe(CN)_6]$. The other parameters remain unchanged.

1.2 Synthesis of the amorphous oxycyanide pre-catalysts

For the synthesis of high-entropy amorphous **HE-CNO**, 100 mg HE-PBA precursor was placed in a porcelain boat and heated to 200 °C in air in a tube furnace at a heating rate of 10 °C min^{-1}, and maintained for 2 h. After that, the porcelain boat was cooled, and the powdery product was collected. The synthesis procedures of the

counterparts, namely, CoFeCuMn-CNO, CoFeCu-CNO, CuFe-CNO and Fe-CNO, were the same as the fabrication of HE-CNO, where the precursors were replaced by the quaternary, ternary, binary PBAs and unary PB nanocube precursors, respectively.

1.3 Structural characterizations

The X-ray diffraction (XRD) was performed on a Philips X'Pert Pro Super diffractometer with Cu Kα radiation (λ = 1.54178 Å). The Fourier transform infrared (FT-IR) spectra were measured on MAGNA-IR 750 (Nicolet Instrument). The scanning electron microscopy (SEM) images were taken on a JEOL JSM-6700F SEM. The transmission electron microscopy (TEM) was carried out on a JEM-2100F field emission electron microscope at an acceleration voltage of 200 kV. The high-resolution TEM (HRTEM), high-angle annular dark-field scanning transmission electron microscopy (HAADF-STEM) and corresponding elemental mapping analyses were performed on a Thermo Fischer Talos F200X TEM. The nitrogen adsorption-desorption isotherms were carried out by using a Micromeritics ASAP 2460 system, and all the gas adsorption experiments were performed at liquid-nitrogen temperature (77 K) after degassed at 300 °C for 6 h. The atomic ratio of the metals was determined by inductively coupled plasma optical emission spectrum (ICP-OES) on a Perkin Elmer Optima 7300DV ICP emission spectroscope. The X-ray photoelectron spectroscopy (XPS) analyses were performed on a VGESCALAB MKII X-ray photoelectron spectrometer with an excitation source of Mg Kα = 1253.6 eV, and the resolution level was lower than 1 atom%.

1.4 Electrocatalytic study

All the electrochemical measurements were performed in a three-electrode system linked with an electrochemical workstation (Ivium Vertex. C. EIS). All potentials were calibrated to a reversible hydrogen electrode (RHE) according to the Nernst equation and the data were presented without iR correction. Typically, 4 mg of catalyst and 50 μL Nafion solution (Sigma Aldrich, 5 wt%) were dispersed in 1 mL water-isopropanol mixed solution (volume ratio of 3:1) by sonicating for at least 30

min to form a homogeneous ink. Then 5 μL of the dispersion (containing 20 μg of catalyst) was loaded onto a glassy carbon electrode with 3 mm diameter, resulting in a catalyst loading of 0.285 mg cm^{-2}. The as-prepared catalyst film was allowed to be dried at room temperature. The cyclic voltammetry (CV) and linear sweep voltammetry (LSV) with a scan rate of 2 mV s^{-1} were conducted in O_2-purged 1 M KOH solution. A Hg/HgO electrode was used as the reference electrode, a platinum gauze electrode (2 cm × 2 cm, 60 mesh) was used as the counter electrode, and the glassy carbon electrodes loaded with various catalysts were served as the working electrodes. The Faradaic efficiency (FE) was measured at a constant anodic current of 20 mA. The electrochemical impedance spectroscopy (EIS) measurements were operated in the same configuration at 1.6 V vs. RHE from 10^{-2}-10^5 Hz. The EIS data were fitted according to the following equivalent circuit, where R_s, R_{ct} and R_{int} are the series resistance, charge-transfer resistance, and solid-electrolyte interface resistance, respectively; CPE_1 and CPE_2 correspond to the capacitances derived from the solid-electrolyte interface process and the Faradic process.

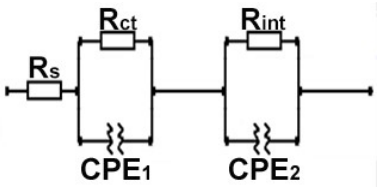

2. Additional physical and electrochemical characterizations

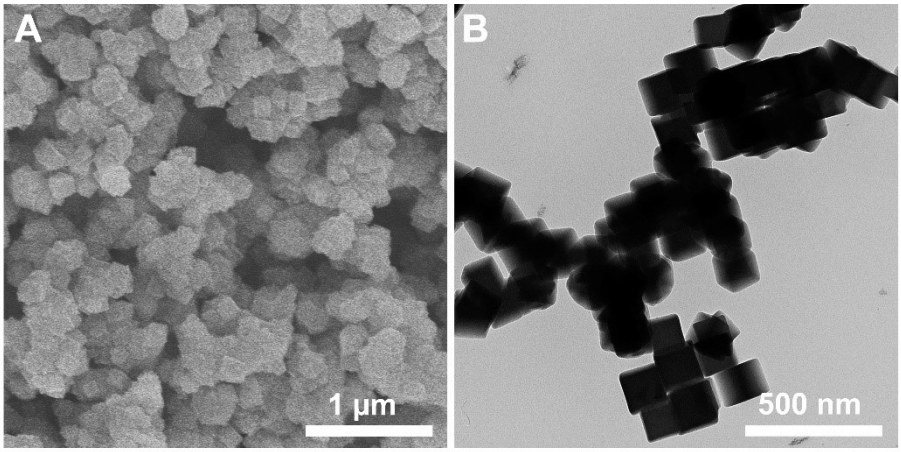

Fig. S1 (A) SEM and (B) TEM images of HE-PBA nanocube precursor.

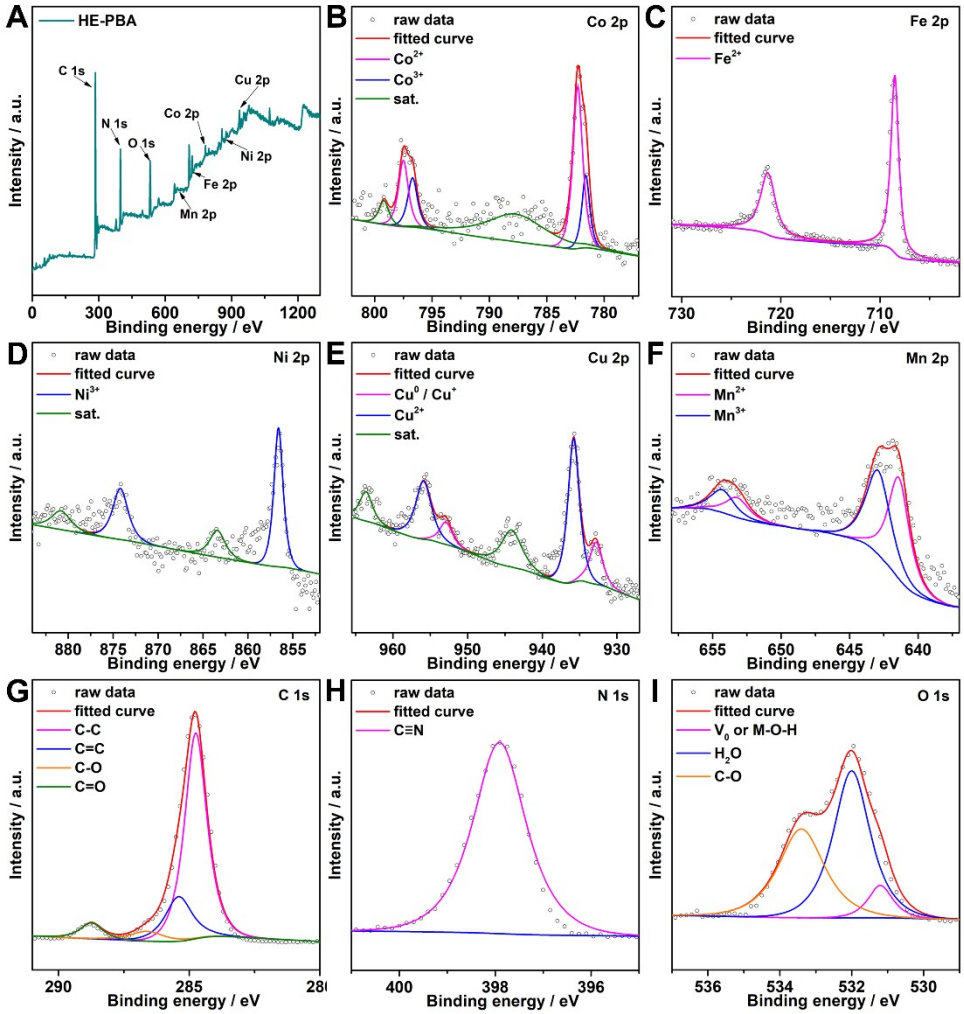

Fig. S2 XPS spectra of the HE-PBA nanocube precursor. (A) Survey spectra. (B-I) XPS spectra of Co, Fe, Ni, Cu, Mn, C, N and O, respectively.

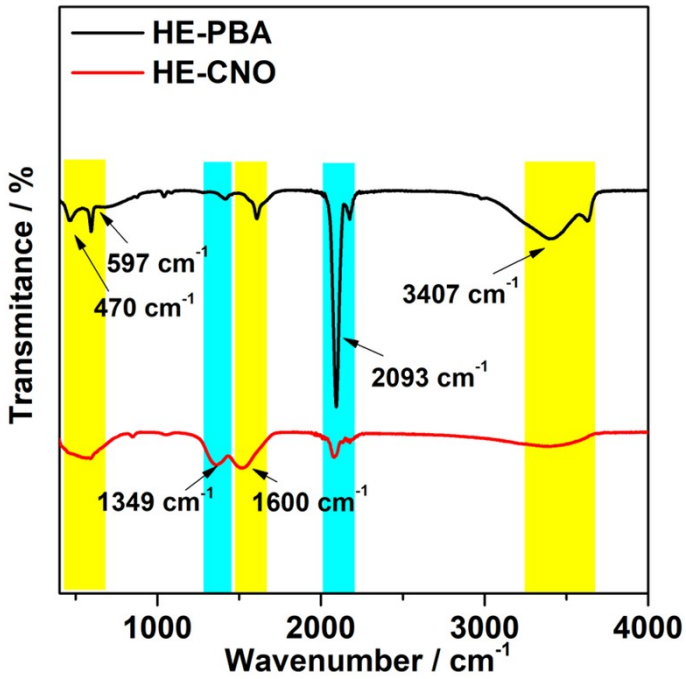

Fig. S3 FT-IR spectra of HE-PBA precursor and HE-CNO.

The structural characteristics of HE-PBA and HE-CNO were investigated by Fourier transform infrared spectroscopy (FT-IR). As shown in Fig. S3, the peaks centered at 1600 cm^{-1} and 3407 cm^{-1} can be attributed to the tensile and in-plane deformation of -OH, indicating the presence of water molecules.[1, 2] In the case of the HE-PBA, the absorption peaks of -OH can be assigned to the tensile vibration of water molecules bound to the metal ions, corresponding to the coordinated water in PBA lattice.[3, 4] The high-intensity band at 2093 cm^{-1} can be assigned to the C≡N stretching vibration, while such signal significantly declined for the HE-CNO, indicating that the oxidation process could effectively break the C≡N bonds.[1, 2] Besides, the peaks at 470 cm^{-1} corresponding to C-M bonds also show obvious decrement after the oxidation process, while in contrast, the peaks located at 597 cm^{-1} and 1349 cm^{-1} corresponding to O-M bonds and C-O tensile deformation increase emerge along with the oxidation, suggesting the formation of oxide species during the thermal oxidation progress.[5-8]

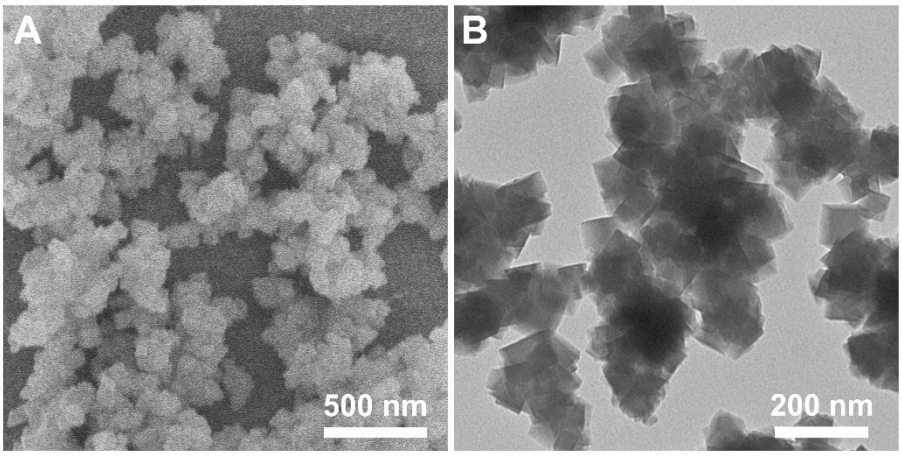

Fig. S4 (A) SEM and (B) TEM images of the quaternary CoFeCuMn-CNO.

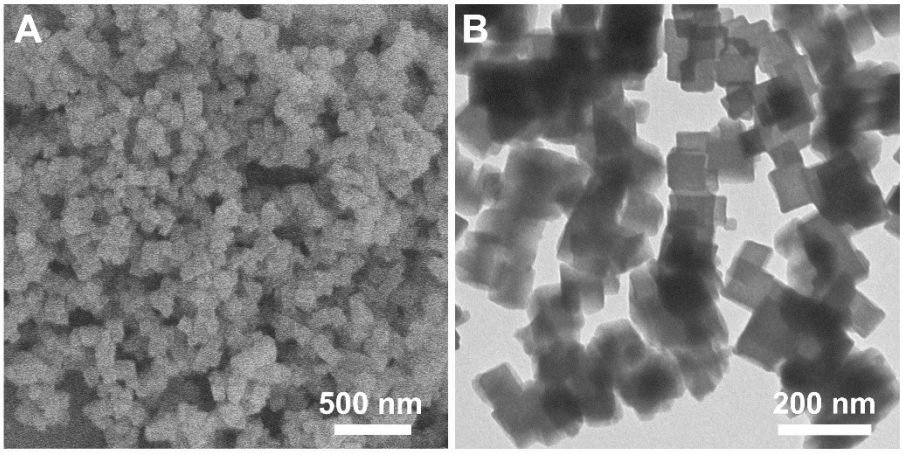

Fig. S5 (A) SEM and (B) TEM images of the ternary CoFeCu-CNO.

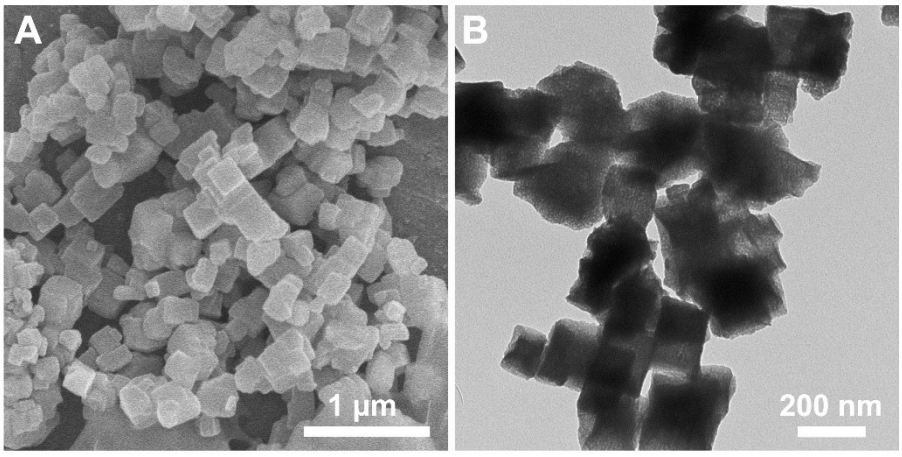

Fig. S6 (A) SEM and (B) TEM images of the binary CuFe-CNO.

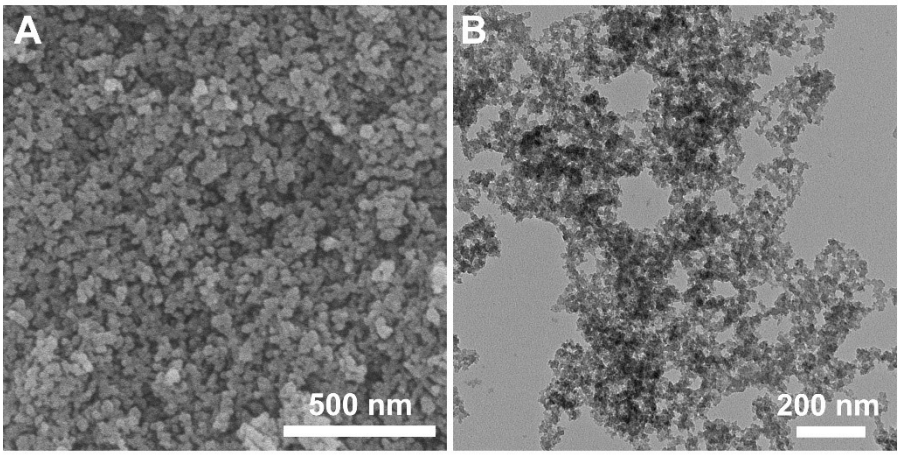

Fig. S7 (A) SEM and (B) TEM images of the unary Fe-CNO.

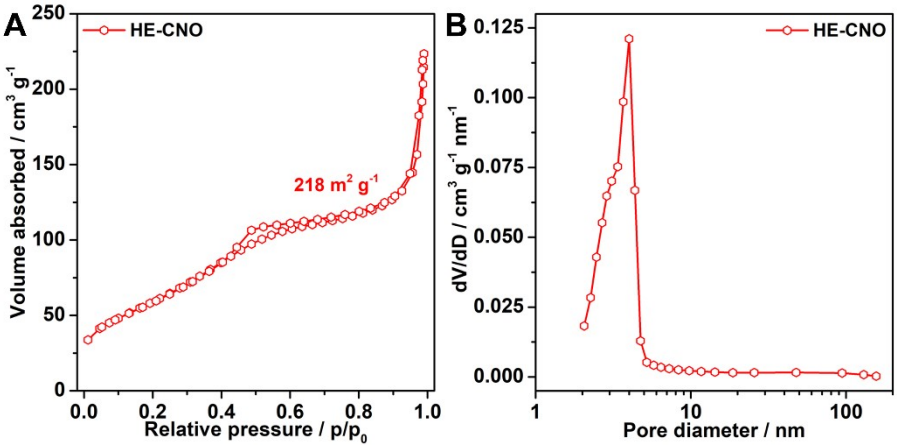

Fig. S8 (A) Nitrogen adsorption-desorption isotherm and the calculated BET specific surface area of HE-CNO. (B) Pore size distribution.

Table S1 Comparison of the OER performance. All the data were obtained in 1 M KOH electrolyte, and the catalysts were in powdery form without loading on porous and conductive supports.

	η_{10} [mV]	$j_{geo}@\eta_{500mV}$ [mA cm^{-2}]	$j_{Cdl}@\eta_{400mV}$ [A F^{-1}]	Stability	Ref.
HE-PBA	—	2.1	18.2	—	this work
HE-CNO	**328**	**137.5**	**283.6**	**1220%@72 h**	this work
HE-CNO-pc	**278**	**216.8**	**556.8**	—	this work
CoFeCuMn-CNO	366	63.7	145.0	—	this work
CoFeCu-CNO	388	28.6	114.2	—	this work
CuFe-CNO	503	9.8	17.8	—	this work
Fe-CNO	—	5.5	21.5	—	this work
$(Ni_{0.62}Fe_{0.38})_2P$ hollow nanocube derived from PBA	290	—	—	80.5%@10 h	9
Ni-Co oxide nanocage derived from PBA	380	—	~0.3	100%@10 h	10
FeCoNi-P derived from PBA	265	—	~14.8	—	11
Dodecagon N-doped Pd-CoNi-C nanosheet derived from PBA	309	104.0	~0.3	—	12
$CoFe_2O_4$ nanosheet derived from PBA	275	88.9	1.3	87.5%@10 h	13
CoNiFe PBA (Co/Ni = 1:3)	320	—	21.7	—	14
CoFeZn PBA	343	92.6	0.5	82.6%@12 h	15
Defective Co PBA	400	70.0	0.08	72%@10000 s	16
$Co_3S_4@MoS_2$ hollow heterostructure derived from PBA	280	—	—	87.5%@2000 cycles /90.2%@10 h	17
$Fe_{0.5}Co_{0.5}MoO_{4-x}S_x$ nanoflower derived from PBA	263	—	—	97.5%@1000 cycles /~87%@72 h	18
Co/CoTe microcube derived from PBA	337	231.2	2.0	94.8%1000 cycles	19
Pt-decorated NiFe PBA nanocube	333	80.5	11.0	99.6%@1000 cycles /85.6%@12 h	20
CoCo PBA nanocube	329	126.6	270.0	499.1%@60 h	21
CoFe PBA nanocube	463	19.6	22.0	205%@60 h	21

Fe PB nanocube	528	7.8	19.0	151%@60 h	21
NiFe PBA nanocube	587	3.2	8.0	114%@60 h	21
Ni-P porous nanoplate/C derived from PBA	300	—	—	74.1%@1000 cycles /~102.1%@10 h	22
$CoSe_2$ nanobox derived from PBA	335	—	2.0	94.4%@1000 cycles /~91%@4 h	23
Fe-doped CoP core-shell nanocage derived from PBA	300	—	—	101.9%@1000 cycles /~37.8%@12 h	24
CoFe/$CoFeO_x$ derived from PBA embedded in N-C	330	—	4.5	92.5%@2000 cycles /~59.3%@20 h	25
CoFe PBA hollow cage	330	—	0.2	97.2%@5000 cycles /~82.7%@12 h	26
Partially phosphated Fe-doped CoP derived from PBA	262	79.4	1.8	95.0%@3000 cycles /96.0%@18 h	27
CoFe oxide nanoframe derived from PBA	290	—	—	94.8%@500 cycles	28
MnFe PBA@ $H_3PMo_{12}O_{40}$ hollow nanocube	440	—	0.3	—	29
RuO_2	340	52.0	—	—	30
IrO_2	320	50.0	2.9	72.9%@1000 cycles	31

Table S2 The fitted R_s and R_{ct} values of the catalysts.

	R_s [Ω]	**R_{ct} [Ω]**
HE-PBA	7.8	1190.0
HE-CNO	0.7	24.8
CoFeCuMn-CNO	2.1	41.1
CoFeCu-CNO	0.5	277.9
CuFe-CNO	6.9	826.1
Fe-CNO	0.8	1110.0

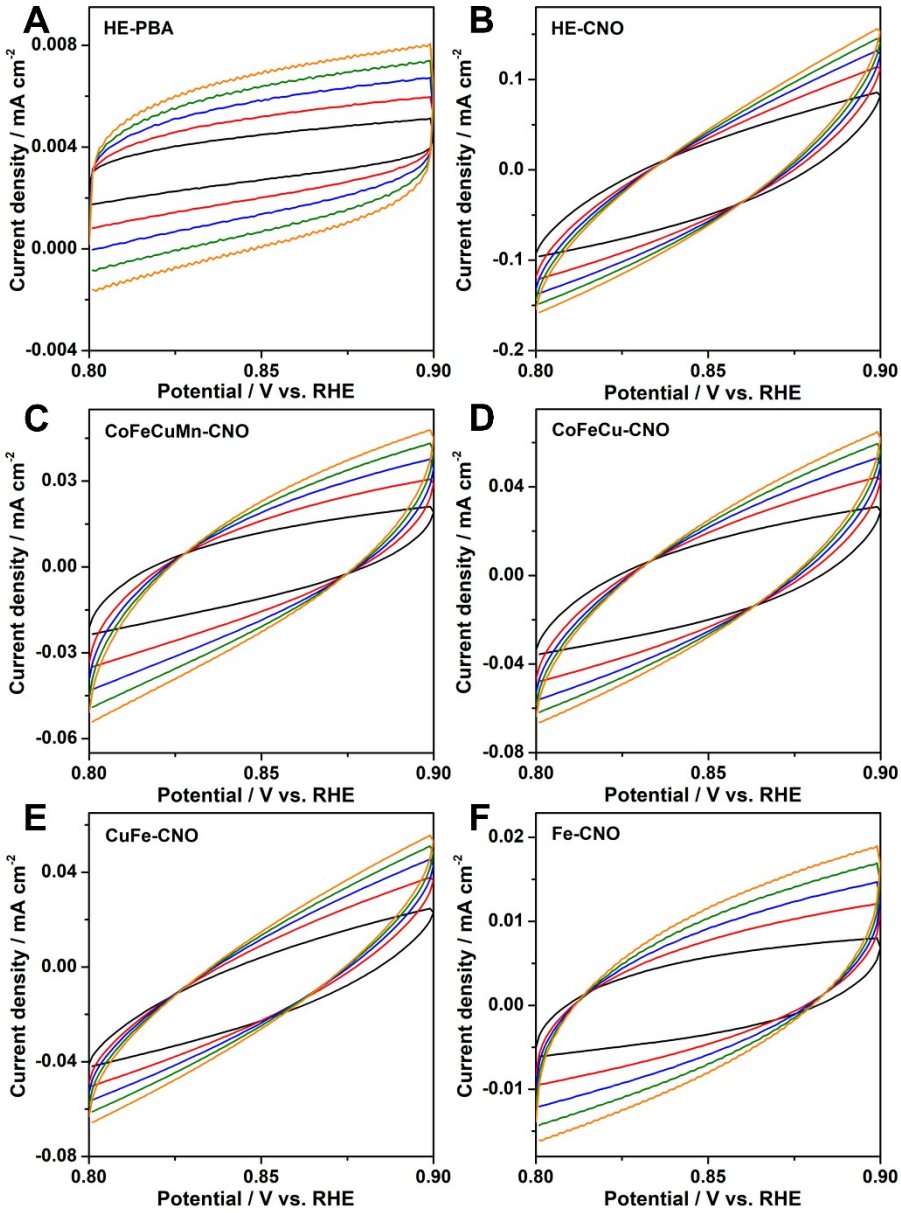

Fig. S9 CV curves in the non-redox region for the estimation of electrochemical double-layer capacitance (C_{dl}).

The estimation of the effective active surface area of the samples was carried out according to literature.[32, 33] Cyclic voltammetry (CV) was performed in O_2-degassed 1 M KOH solution at various scan rates (20, 40, 60, 80 and 100 mV s^{-1}) in the range of 0.8-0.9 V vs. RHE (Fig. S9). The C_{dl} values can be determined by plotting the Δj (j_{anode}-$j_{cathode}$) at 0.85 V vs. RHE against the scan rate (Fig. 3D), where the slope is twice C_{dl}. The C_{dl} values are expected to be linearly proportional to the effective surface area.

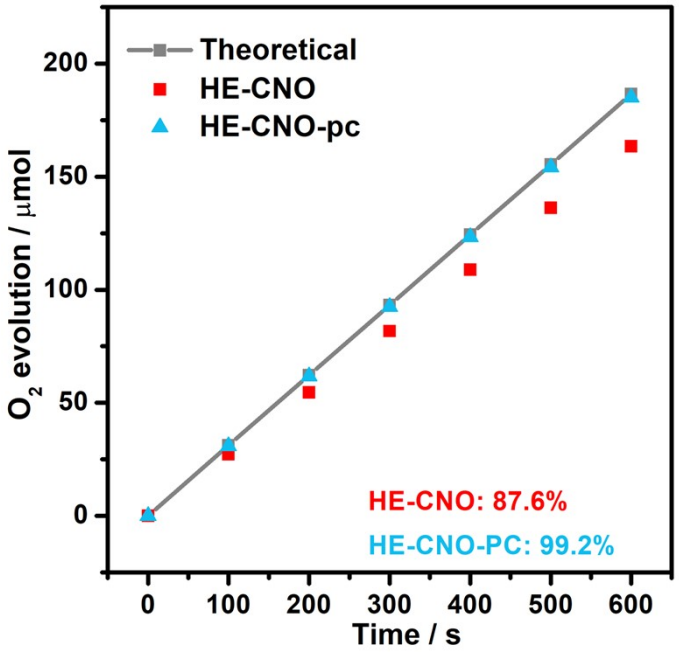

Fig. S10 The calculated Faradaic efficiency of HE-CNO and HE-CNO-pc.

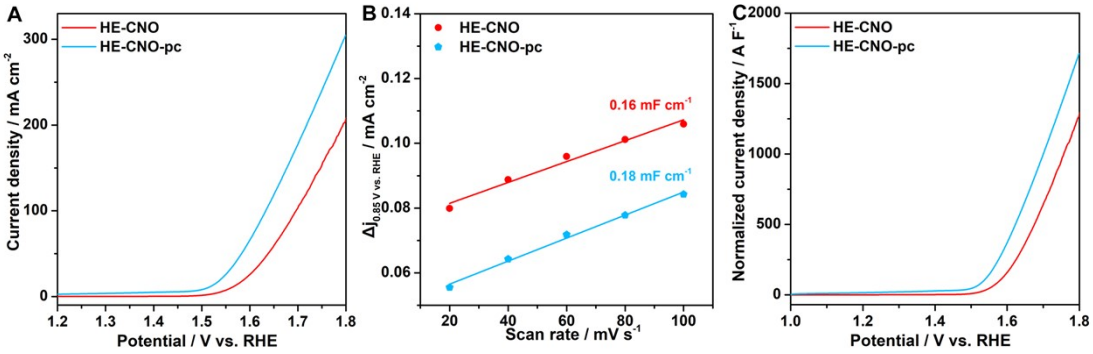

Fig. S11 Comparison of the electrochemical parameters of HE-CNO before and after stability test. (A) LSV curves. (B) C_{dl} values. (C) C_{dl}-normalized activity.

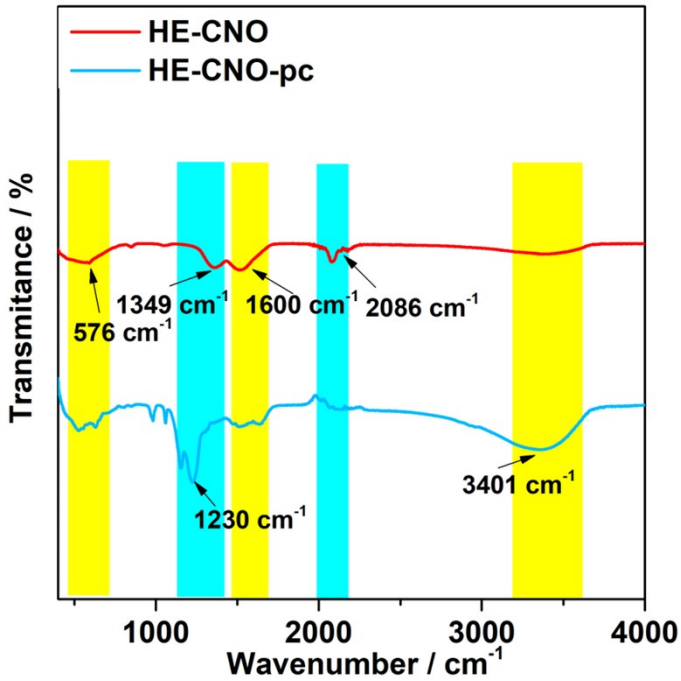

Fig. S12 FT-IR spectra of HE-CNO before and after stability test.

The FT-IR spectra were conducted to study the structural characteristics of HE-CNO before and after the stability test. As shown in Fig. S12, the peaks centered at 1600 cm^{-1} and 3401 cm^{-1} can be attributed to the tensile and in-plane deformation of -OH.[1, 2] In the case of HE-CNO, the band at 2086 cm^{-1} can be assigned to the C≡N stretching, while the peak vanished after the stability test, indicating the complete oxidation of the cyan group during the pre-oxidation process.[3, 4] Besides, the intensity of peak at 576 cm^{-1} increases after the stability test, indicating the enhanced O-M bonding owing to the formation of the catalytically active metal (oxy)hydroxides.[6] In addition, the emerging peak at 1230 cm^{-1} can be assigned to the C-C bonds owing to the addition of Nafion solution in the electrochemical test.[34]

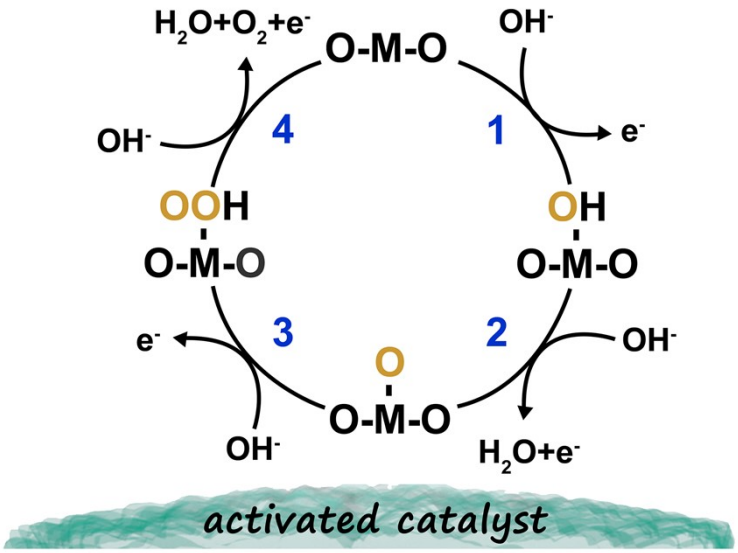

Fig. S13 Possible OER mechanism on the surface of the activated HE-CNO. The activated HE-CNO could offer more catalytically active high-valence sites for OER owing to the efficient pre-oxidation process, which is responsible for the substantially increased OER activity during the long-term operation.

Reference

1. D. Sun, H. Wang, B. Deng, H. Zhang, L. Wang, Q. Wan, X. Yan and M. Qu, *Carbon*, 2019, **143**, 706-713.
2. B. Xie, P. Zuo, L. Wang, J. Wang, H. Huo, M. He, J. Shu, H. Li, S. Lou and G. Yin, *Nano Energy*, 2019, **61**, 201-210.
3. Y. Chen, X. Huang, D. Sun, H. Ma, G. Wang, C. Ma and J. Hao, *Sep. Purif. Technol.*, 2021, **277**, 119468.
4. C. L. C. Carvalho, A. T. B. Silva, R. A. S. Luz, G. M. B. Castro, C. da Luz Lima, V. R. Mastelaro, R. R. da Silva, O. N. Oliveira and W. Cantanhêde, *ACS Appl. Nano Mater.*, 2018, **1**, 4283-4293.
5. J. Zhai, Q. Kang, Q. Liu, D. Lai, Q. Lu and F. Gao, *J. Colloid Interface Sci.*, 2022, **608**, 1942-1950.
6. A. Pramanik, S. Maiti and S. Mahanty, *Dalton Trans.*, 2015, **44**, 14604-14612.
7. G. Tao and J. Wang, *Carbon*, 2018, **133**, 209-217.
8. H. N. Miankushki, A. Sedghi and S. Baghshahi, *J. Solid State Electrochem.*,

2018, **22**, 3317-3329.

9. H.-H. Zou, C.-Z. Yuan, H.-Y. Zou, T.-Y. Cheang, S.-J. Zhao, U. Y. Qazi, S.-L. Zhong, L. Wang and A.-W. Xu, *Catal. Sci. Technol.*, 2017, **7**, 1549-1555.
10. L. Han, X.-Y. Yu and X. W. Lou, *Adv. Mater.*, 2016, **28**, 4601-4605.
11. Y. Du, X. Ding, M. Han and M. Zhu, *ChemCatChem*, 2020, **12**, 4339-4345.
12. H. Zhang, Q. Jiang, J. H. L. Hadden, F. Xie and D. J. Riley, *Adv. Funct. Mater.*, 2021, **31**, 2008989.
13. H. Fang, T. Huang, D. Liang, M. Qiu, Y. Sun, S. Yao, J. Yu, M. M. Dinesh, Z. Guo, Y. Xia and S. Mao, *J. Mater. Chem. A*, 2019, **7**, 7328-7332.
14. M. Ren, J. Lei, J. Zhang, B. I. Yakobson and J. M. Tour, *ACS Appl. Mater. Interfaces*, 2021, **13**, 42715-42723.
15. H. Zou, X. Liu, K. Wang, Y. Duan, C. Wang, B. Zhang, K. Zhou, D. Yu, L.-Y. Gan and X. Zhou, *Chem. Commun.*, 2021, **57**, 8011-8014.
16. Y. Kang, S. Wang, K. S. Hui, H. F. Li, F. Liang, X. L. Wu, Q. Zhang, W. Zhou, L. Chen, F. Chen and K. N. Hui, *Mater. Today Energy*, 2021, **20**, 100572.
17. Y. Guo, J. Tang, Z. Wang, Y.-M. Kang, Y. Bando and Y. Yamauchi, *Nano Energy*, 2018, **47**, 494-502.
18. B. Fei, Z. Chen, Y. Ha, R. Wang, H. Yang, H. Xu and R. Wu, *Chem. Eng. J.*, 2020, **394**, 124926.
19. R. Yoo, K. Min, H. Kim, D. Lim and S.-H. Baeck, *Appl. Surf. Sci.*, 2022, **581**, 152405.
20. M. Fu, Q. Zhang, Y. Sun, G. Ning, X. Fan, H. Wang, H. Lu, Y. Zhang and H. Wang, *Int. J. Hydrogen Energy*, 2020, **45**, 20832-20842.
21. W. Sun, Z. Wei, J. Qi, L. Kang, J. Li, J. Xie, B. Tang and Y. Xie, *Chin. J. Chem.*, 2021, **39**, 2347-2353.
22. X.-Y. Yu, Y. Feng, B. Guan, X. W. Lou and U. Paik, *Energy Environ. Sci.*, 2016, **9**, 1246-1250.
23. V. Ganesan and J. Kim, *Mater. Lett.*, 2018, **223**, 49-52.
24. J.-Y. Xie, Z.-Z. Liu, J. Li, L. Feng, M. Yang, Y. Ma, D.-P. Liu, L. Wang, Y.-

M. Chai and B. Dong, *J. Energy Chem.*, 2020, **48**, 328-333.

25. M. Hou, S. Gong, L. Ji, J. Huang, M. Xu and Z. Chen, *Chem. Eng. J.*, 2021, **419**, 129575.
26. Y. Feng, X. Wang, P. Dong, J. Li, L. Feng, J. Huang, L. Cao, L. Feng, K. Kajiyoshi and C. Wang, *Sci. Rep.*, 2019, **9**, 15965.
27. Q. Yang, H. Dai, W. Liao, X. Tong, Y. Fu, M. Qian and T. Chen, *Dalton Trans.*, 2021, **50**, 18069-18076.
28. J. Nai, J. Zhang and X. W. Lou, *Chem*, 2018, **4**, 1967-1982.
29. Y. Wang, Y. Wang, L. Zhang, C.-S. Liu and H. Pang, *Chem. Asian J.*, 2019, **14**, 2790-2795.
30. M. Zhu, Z. Zhang, H. Zhang, H. Zhang, X. Zhang, L. Zhang and S. Wang, *J. Colloid Interface Sci.*, 2018, **509**, 522-528.
31. K. Lu, T. Gu, L. Zhang, Z. Wu, R. Wang and X. Li, *Chem. Eng. J.*, 2021, **408**, 127352.
32. M. A. Lukowski, A. S. Daniel, F. Meng, A. Forticaux, L. Li and S. Jin, *J. Am. Chem. Soc.*, 2013, **135**, 10274-10277.
33. J. Xie, J. Zhang, S. Li, F. Grote, X. Zhang, H. Zhang, R. Wang, Y. Lei, B. Pan and Y. Xie, *J. Am. Chem. Soc.*, 2013, **135**, 17881-17888.
34. Y. Lin, H. Wang, C. K. Peng, L. Bu, C. L. Chiang, K. Tian, Y. Zhao, J. Zhao, Y. G. Lin, J. M. Lee and L. Gao, *Small*, 2020, **16**, e2002426.